
COSMOS: CONTINUOUS SIMPLICIAL NEURAL NETWORKS

Aref Einizade
LTCI, Télécom Paris
Institut Polytechnique de Paris
aref.einizade@telecom-paris.fr

Dorina Thanou
EPFL, Lausanne, Switzerland
dorina.thanou@epfl.ch

Fragkiskos D. Malliaros
CentraleSupélec, Inria
Université Paris-Saclay
fragkiskos.malliaros@centralesupelec.fr

Jhony H. Giraldo
LTCI, Télécom Paris
Institut Polytechnique de Paris
jhony.giraldo@telecom-paris.fr

ABSTRACT

Simplicial complexes provide a powerful framework for modeling high-order interactions in structured data, making them particularly suitable for applications such as trajectory prediction and mesh processing. However, existing simplicial neural networks (SNNs), whether convolutional or attention-based, rely primarily on discrete filtering techniques, which can be restrictive. In contrast, partial differential equations (PDEs) on simplicial complexes offer a principled approach to capture continuous dynamics in such structures. In this work, we introduce **continuous simplicial neural networks (COSMOS)**, a novel SNN architecture derived from PDEs on simplicial complexes. We provide theoretical and experimental justifications of COSMOS’s stability under simplicial perturbations. Furthermore, we investigate the over-smoothing phenomenon—a common issue in geometric deep learning—demonstrating that COSMOS offers better control over this effect than discrete SNNs. Our experiments on real-world datasets of ocean trajectory prediction and regression on partial deformable shapes demonstrate that COSMOS achieves competitive performance compared to state-of-the-art SNNs in complex and noisy environments.

Keywords Simplicial Neural Networks · Partial Differential Equations · Over-smoothing · Stability.

1 Introduction

Graph representation learning provides a powerful framework for modeling structured data. In this context, graph neural networks (GNNs) have gained significant attention [1, 2, 3, 4], extending neural network architectures to graph-structured data. By capturing complex relationships between nodes, GNNs have been successfully applied to various domains, including semi-supervised learning [3], social network analysis [5], drug discovery [6], materials modeling [7], and computer vision [8, 9].

However, traditional GNNs primarily focus on pairwise interactions between nodes, limiting their ability to model higher-order relationships in complex systems such as biological networks [10]. Continuous models play a crucial role in capturing real-world dynamics of data evolving on structured data [11]. Compared to their discrete counterparts, continuous convolutional models offer several advantages, including: (i) better control of over-smoothing [11], preventing excessive feature homogenization across the structure, and (ii) greater robustness to structural perturbations [12, 13]. To take account for the higher-order interactions, the limitation, researchers have explored more expressive mathematical structures, such as *abstract simplicial complexes* [14, 15], which generalize graphs by incorporating multi-way connections between elements.

An abstract simplicial complex is a combinatorial structure composed of sets that are closed under subset operations. For instance, a three-dimensional simplicial complex includes tetrahedrons (four-element sets), triangles (three-element sets), edges (two-element sets), and vertices (one-element sets), as illustrated in Fig. 1. Graphs correspond to simplicial

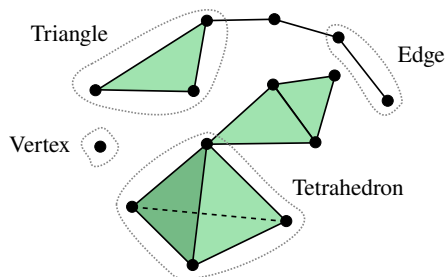


Figure 1: Example of an abstract simplicial complex.

1-complexes, containing only nodes and edges, while point clouds (sets of unconnected nodes) can be seen as simplicial 0-complexes. Throughout this paper, the term “simplicial complexes” refers specifically to abstract simplicial complexes.

Building upon this mathematical foundation, simplicial neural networks (SNNs) [16] have emerged as a powerful approach for learning on higher-order structures. Most existing SNNs rely on discrete simplicial filters [16, 17] and their variations [18] to process data defined on simplicial complexes. However, a fundamental question remains largely unexplored: *how can we design continuous SNNs?* Despite the benefits of traditional GNNs, to the best of our knowledge, no continuous filtering method has been proposed for learning on simplicial complexes. To address this gap, we introduce **continuous simplicial neural networks (COSMOS)**, the first method for modeling continuous dynamics of simplicial complexes with higher-order connections. We analyze COSMOS both theoretically and empirically, demonstrating its effectiveness in learning from simplicial complex data. Our main contributions can be summarized as follows:

- We propose COSMOS, a novel approach based on partial differential equations (PDEs) defined on simplicial complexes. This formulation enables continuous information propagation across simplicial structures.
- We establish theoretical stability guarantees for COSMOS, demonstrating its robustness to structural perturbations.
- We provide a detailed analysis of the over-smoothing phenomenon in both discrete and continuous SNNs, showing that COSMOS achieves a better control on the rate of convergence to the over-smoothing state.
- We validate COSMOS through experiments on both synthetic and real-world datasets, showing its competitive performance against state-of-the-art methods.

2 Related Work

The introduction of topological signal processing over simplicial complexes [14] has significantly advanced topological methods in machine learning, highlighting the benefits of these data structures [15]. This progress has driven the development of neural network architectures capable of processing simplicial complexes, contributing to the emerging field of topological deep learning [19, 20]. The evolution of the simplicial neural network architectures has followed a trajectory similar to that of GNNs, with the following stages: *i)* the establishment of principles in *topological signal processing over simplicial complexes* [14], *ii)* the formulation of *simplicial filters* [16], *iii)* the application of these filters to create *SNNs* [3, 16], and *iv)* the development of *simplicial attention mechanisms* [4, 21].

Research on learning methods for simplicial complexes has explored various approaches. [22] were among the first to develop neural networks that operate on the edges of graphs using simplicial representations. Building on this, [16] incorporated the Hodge Laplacian, a generalization of the graph Laplacian, to extend GNNs to higher-dimensional simplices, enabling better modeling of their relationships. [23] and [24] refined this approach by separating the lower and upper Laplacians—two components of the Hodge Laplacian that capture connections between simplices of different dimensions—to perform multi-order convolutions. [25] further extended the framework in [23] to detect topological holes, while [26] integrated node and edge operations for link prediction. More recently, attention mechanisms have been incorporated into simplicial networks [10, 21, 27].

Most of these studies focus on learning within individual simplicial levels without explicitly modeling the incidence relations (interactions between simplices of different dimensions) inherent in simplicial complexes. The inclusion of these relations was explored by [28] and [29], which proposed convolutional-like architectures that were later unified under the simplicial complex convolutional neural network (SCCNN) framework [30, 31]. Simultaneously, [18] and [32] extended message-passing techniques from GNNs [33] to simplicial complexes by leveraging both adjacency and incidence structures.

Unlike GNNs, the theoretical understanding of SNNs is still developing. For example, [23] analyzed how permutation-symmetric neural networks preserve equivariance under permutation and orientation changes—an important property also supported by SCCNNs. In another study, [18] examined message-passing in simplicial complexes through the lens of the Weisfeiler-Lehman test, applied to simplicial complexes derived from clique expansions of graphs. Additionally, [24] proposed a spectral formulation based on the simplicial complex Fourier transform.

In contrast to previous methods, COSMOS leverages continuous dynamics in both the lower and upper Hodge Laplacians. Although the SCCNN framework also decouples the Hodge Laplacians in a discrete setting, it faces two challenges: (i) the order of the Hodge filters must be manually tuned, and (ii) the model has limited control over over-smoothing, a common issue in deep GNNs and SNNs. COSMOS addresses these challenges by introducing PDEs on simplicial complexes, which enable differentiability of the convolutional operation with respect to the simplicial receptive fields, providing greater flexibility and robustness in learning.

3 Preliminaries

3.1 Notation and Simplicial Complexes

Notation. Calligraphic letters like \mathcal{X} designate sets, and $|\mathcal{X}|$ represents their cardinality. Uppercase boldface letters such as \mathbf{B} represent matrices, and lowercase boldface letters like \mathbf{x} denote vectors. Similarly, $\text{tr}(\cdot)$ represents the trace of a matrix, $\|\cdot\|$ is the ℓ_2 -norm of a vector, and $(\cdot)^\top$ designates transposition.

Simplicial complex. A simplicial complex is a set \mathcal{X} of finite subsets of another set \mathcal{V} that is closed under restriction, i.e., $\forall s^k \in \mathcal{X}$, if $s^{k'} \subseteq s^k$, then $s^{k'} \in \mathcal{X}$. Each element of \mathcal{X} is called a *simplex*. Particularly, if $|s^k| = k + 1$, we call s^k a k -simplex. A *face* of s^k is a subset with cardinality k , while a *coface* of s^k is a $k + 1$ -simplex that has s^k as a face. We refer to the 0-simplices as nodes, the 1-simplices as edges, and the 2-simplices as triangles. For higher-order simplices, we use the term k -simplices. The notation \mathcal{X}_k represents the collection of k -simplices of \mathcal{X} . If $\mathcal{X}_c = \emptyset \forall c > d$, we say \mathcal{X} is a simplicial complex of dimension d . For example, a simple graph is a simplicial complex of dimension one and can be represented as $G = (\mathcal{X}_0, \mathcal{X}_1)$, i.e., the set of nodes and edges.

We use incidence matrices $\mathbf{B}_k \in \{-1, 0, 1\}^{|\mathcal{X}_{k-1}| \times |\mathcal{X}_k|}$, to describe the incidence relationships between $k - 1$ -simplices (faces) and k -simplices. For example, \mathbf{B}_1 and \mathbf{B}_2 are node-to-edge and edge-to-triangle incidence matrices, respectively. Simplicial complexes are defined with some orientation, and therefore the value $\mathbf{B}_k(i, j)$ is either -1 or 1 if the k -simplex i is incident to the $k - 1$ -simplex j depending on the orientation, and 0 otherwise. Please notice that \mathbf{B}_0 is not defined. We define the k -Hodge Laplacians as:

$$\mathbf{L}_k = \mathbf{B}_k^\top \mathbf{B}_k + \mathbf{B}_{k+1} \mathbf{B}_{k+1}^\top, \quad (1)$$

where $\mathbf{L}_{k,d} = \mathbf{B}_k^\top \mathbf{B}_k$ is the *lower Laplacian*, $\mathbf{L}_{k,u} = \mathbf{B}_{k+1} \mathbf{B}_{k+1}^\top$ is the *upper Laplacian*, $\mathbf{L}_0 = \mathbf{B}_1 \mathbf{B}_1^\top$ is the *graph Laplacian*, and $\mathbf{L}_d = \mathbf{B}_d^\top \mathbf{B}_d$. Common SNNs [30] define their convolution operations as matrix polynomials of the Hodge Laplacians in (1) over *simplicial signals*, which are signals defined over the simplicial complex.

Simplicial signal. We define a k -simplicial signal as a function in \mathcal{X}_k as $x_k : \mathcal{X}_k \rightarrow \mathbb{R}$. Therefore, we can define a one-dimensional k -simplicial signal as $\mathbf{x}_k \in \mathbb{R}^{|\mathcal{X}_k|}$. We can calculate how \mathbf{x}_k varies w.r.t. the faces and cofaces of k -simplices by $\mathbf{B}_k \mathbf{x}_k$ and $\mathbf{B}_{k+1}^\top \mathbf{x}_k$ [31]. For example, in a node signal \mathbf{x}_0 , $\mathbf{B}_1^\top \mathbf{x}_0$ computes its *gradient* as the difference between adjacent nodes, and in an edge signal \mathbf{x}_1 , $\mathbf{B}_1 \mathbf{x}_1$ computes its *divergence* [31].

Dirichlet energy. The Dirichlet energy $E(\cdot)$ quantifies the smoothness of a simplicial signal with respect to the k -Hodge Laplacian. A lower energy value indicates a smoother signal, with zero energy corresponding to a constant signal across all connected simplices.

Definition 3.1 ([30, 31]). The Dirichlet energy of a simplicial signal \mathbf{x}_k can be stated as:

$$E(\mathbf{x}_k) := \mathbf{x}_k^\top \mathbf{L}_k \mathbf{x}_k = \|\mathbf{B}_k \mathbf{x}_k\|_2^2 + \|\mathbf{B}_{k+1}^\top \mathbf{x}_k\|_2^2. \quad (2)$$

This definition generalizes the Dirichlet energy from graphs to simplicial complexes. Intuitively, it measures how similar the values assigned to adjacent simplices are, with higher energy indicating greater variation.

Simplicial filters. For a k -simplicial signal \mathbf{x}_k , a simplicial filter is a function $f : \mathbb{R}^{|\mathcal{X}_k|} \rightarrow \mathbb{R}^{|\mathcal{X}_k|}$ given as:

$$f(\mathbf{x}_k) = \left(\sum_{i=0}^{T_d} \alpha_i \mathbf{L}_{k,d}^i + \sum_{i=0}^{T_u} \beta_i \mathbf{L}_{k,u}^i \right) \mathbf{x}_k, \quad (3)$$

where $\{\alpha_0, \dots, \alpha_{T_d}\}$ and $\{\beta_0, \dots, \beta_{T_u}\}$ are the parameters of the polynomials, and T_d, T_u are the order of the polynomials [34]. Please notice that the well-known graph filter [35] is a specific case of (3). In this case, the graph

signal is given by $\mathbf{x}_0 \in \mathbb{R}^{|\mathcal{X}_0|}$ and since \mathbf{B}_0 is not defined, we have $f(\mathbf{x}_0) = \sum_{i=0}^{T_u} \beta_i \mathbf{L}_0^i \mathbf{x}_0$, which is the classical graph filter with the graph Laplacian as the shift operator.

3.2 Discrete Simplicial Neural Network

Typically, a convolutional neural network is composed of filters and non-linearities. For simplicial complexes, we can define an SNN using simplicial filters. However, notice that relying only on filters like in (3) ignores the connections among the adjacent simplices modeled by \mathbf{L}_k . Since different simplicial signals $\mathbf{x}_0, \mathbf{x}_1, \dots, \mathbf{x}_K$ influence each other via the simplicial complex localities, previous works have defined simplicial filter banks [34].

One-dimensional case. Let the lower and upper projections of a simplicial signal \mathbf{x}_k^l at layer l be $\mathbf{x}_{k,d}^l = \mathbf{B}_k^\top \mathbf{x}_{k-1}^l \in \mathbb{R}^{|\mathcal{X}_k|}$ and $\mathbf{x}_{k,u}^l = \mathbf{B}_{k+1} \mathbf{x}_{k+1}^l \in \mathbb{R}^{|\mathcal{X}_k|}$, respectively¹. We can define a simplicial complex layer as a function $g : \mathbb{R}^{|\mathcal{X}_k|} \times \mathbb{R}^{|\mathcal{X}_k|} \times \mathbb{R}^{|\mathcal{X}_k|} \rightarrow \mathbb{R}^{|\mathcal{X}_k|}$ given as:

$$\mathbf{x}_k^l = \sigma \left(\mathbf{H}_{k,d}^l \mathbf{x}_{k,d}^{l-1} + \mathbf{H}_k^l \mathbf{x}_k^{l-1} + \mathbf{H}_{k,u}^l \mathbf{x}_{k,u}^{l-1} \right), \quad (4)$$

where

$$\begin{aligned} \mathbf{H}_{k,d}^l &:= \sum_{i=0}^{T_d} \theta_{k,d,i}^l \mathbf{L}_{k,d}^i, & \mathbf{H}_{k,u}^l &:= \sum_{i=0}^{T_u} \theta_{k,u,i}^l \mathbf{L}_{k,u}^i, \\ \mathbf{H}_k^l &:= \sum_{i=0}^{T_d} \psi_{k,d,i}^l \mathbf{L}_{k,d}^i + \sum_{i=0}^{T_u} \psi_{k,u,i}^l \mathbf{L}_{k,u}^i, \end{aligned} \quad (5)$$

with parameters θ and ψ [31].

Multi-dimensional case. Let $\{\mathbf{X}_k^l, \mathbf{X}_{k,d}^l, \mathbf{X}_{k,u}^l\}$ be the F_{l-1} -dimensional simplicial signal and its lower and upper projections at layer l . Let $\Theta_{k,d,i}^l, \Theta_{k,u,i}^l, \Psi_{k,d,i}^l$, and $\Psi_{k,u,i}^l$ be learnable linear projections in $\mathbb{R}^{F_{l-1} \times F_i}$ corresponding to the α and ϕ parameters for the unidimensional case in (5). Using (3) and (5), we can define an SNN layer for the multidimensional case as follows [31]:

$$\mathbf{X}_k^l = \sigma \left(\sum_{i=0}^{T_d} \mathbf{L}_{k,d}^i \mathbf{X}_{k,d}^{l-1} \Theta_{k,d,i}^l + \sum_{i=0}^{T_d} \mathbf{L}_{k,d}^i \mathbf{X}_k^{l-1} \Psi_{k,d,i}^l + \sum_{i=0}^{T_u} \mathbf{L}_{k,u}^i \mathbf{X}_k^{l-1} \Psi_{k,u,i}^l + \sum_{i=0}^{T_u} \mathbf{L}_{k,u}^i \mathbf{X}_{k,u}^{l-1} \Theta_{k,u,i}^l \right). \quad (6)$$

The discrete SNN in (6) is analogous to the GNN case, where discrete powers of the Hodge Laplacians capture multi-hop diffusions in the simplicial signal and its lower and upper projections.

All the proofs of theorems, propositions, and lemmas of this paper are provided in the Appendix.

4 Continuous Simplicial Neural Network

Discrete SNNs provide flexibility in filtering simplicial signals through lower and upper projections. However, their information propagation remains fixed for each polynomial order, limiting adaptability. In this section, we introduce COSMOS, which enables a dynamic receptive field in each convolutional operation. We begin by formulating the PDEs that govern physics-informed dynamics over simplicial complexes. Next, we define the fundamental operations of COSMOS as the solutions to these PDEs. Finally, we provide a rigorous stability analysis of COSMOS, showing its robustness to topological perturbations in simplicial complexes.

4.1 PDEs in Simplicial Complexes

Our set of PDEs is inspired by heat diffusion on simplicial complexes, providing a natural extension of discrete SNNs. Intuitively, performing heat diffusion over the decoupled Hodge Laplacians enables information propagation at different rates within the continuous domain of the simplicial complex. This parallels the case in regular graphs [11], where continuous GNN formulations have been shown to generalize certain discrete GNNs, opening new possibilities for architectural design.

In our framework, considering both joint, on k -simplex s^k , and independent diffusion processes on s^{k-1} and s^{k+1} allows for greater flexibility in modeling complex relationships. By enabling these dynamics to evolve at different rates,

¹In this work, the superscript l refers to the layer index and should not be confused with exponentiation.

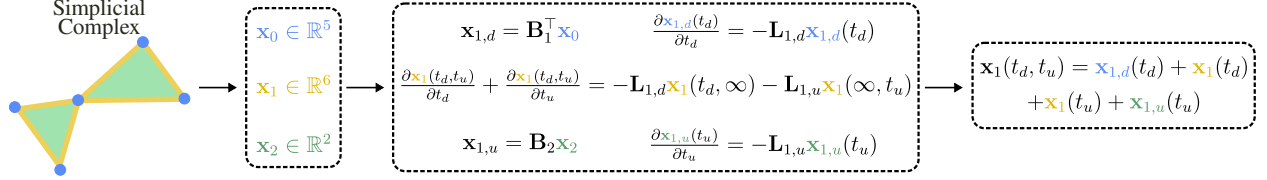


Figure 2: Illustration of the PDE-based signal evolution in a simplicial complex. The dynamics are governed by independent diffusion processes on the lower and upper Hodge Laplacians ($\mathbf{L}_{k,d}$, $\mathbf{L}_{k,u}$) and a coupled process integrating both spaces.

we can better adapt to the underlying topology of the data. Motivated by these considerations, we model simplicial heat diffusion using a system of PDEs on the Hodge Laplacians.

Let t_d and t_u be the time variables governing the dynamics in the lower and upper Laplacians, respectively. We define these dynamics through the following system of PDEs:

- *Independent lower dynamics:* The evolution of the signal in the lower space follows a heat diffusion process:

$$\frac{\partial \mathbf{x}_{k,d}(t_d)}{\partial t_d} = -\mathbf{L}_{k,d} \mathbf{x}_{k,d}(t_d). \quad (7)$$

- *Independent upper dynamics:* Similarly, the signal in the upper space evolves according to:

$$\frac{\partial \mathbf{x}_{k,u}(t_u)}{\partial t_u} = -\mathbf{L}_{k,u} \mathbf{x}_{k,u}(t_u). \quad (8)$$

- *Simultaneous dynamics:* The interaction between the lower and upper spaces is captured by:

$$\begin{aligned} \frac{\partial \mathbf{x}_k(t_d, t_u)}{\partial t_d} + \frac{\partial \mathbf{x}_k(t_d, t_u)}{\partial t_u} \\ = -\mathbf{L}_{k,d} \mathbf{x}_k(t_d, \infty) - \mathbf{L}_{k,u} \mathbf{x}_k(\infty, t_u), \end{aligned} \quad (9)$$

where $\mathbf{x}_k(t_d, \infty) = \lim_{t_u \rightarrow \infty} \mathbf{x}_k(t_d, t_u)$ and $\mathbf{x}_k(\infty, t_u) = \lim_{t_d \rightarrow \infty} \mathbf{x}_k(t_d, t_u)$ state marginal stable solutions in upper and lower subspaces.

- *Integrated dynamics:* The final solution from the contributions of the independent and simultaneous dynamics:

$$\mathbf{x}_k(t_d, t_u) = \mathbf{x}_{k,d}(t_d) + \mathbf{x}_k(t_d) + \mathbf{x}_k(t_u) + \mathbf{x}_{k,u}(t_u). \quad (10)$$

These equations describe the flow of information across different simplicial levels, ensuring a principled integration of both independent and coupled dynamics. Fig. 2 provides a visual representation of these processes for a simplicial complex of dimension 2.

4.2 COSMOS as a Solution to the Simplicial PDEs

We propose COSMOS as a solution to the descriptive sets of PDEs introduced in Section 4.1.

Proposition 4.1. *The solution to the descriptive sets of PDEs in Section 4.1 is given by:*

$$\mathbf{x}'_k(t_d, t_u) = \overbrace{e^{-t_d \mathbf{L}_{k,d}} \mathbf{x}_{k,d}(0)}^{\mathbf{x}_{k,d}(t_d)} + \overbrace{e^{-t_u \mathbf{L}_{k,u}} \mathbf{x}_{k,u}(0)}^{\mathbf{x}_{k,u}(t_u)} + \overbrace{e^{-t_d \mathbf{L}_{k,d}} \mathbf{x}_k(0,0) + e^{-t_u \mathbf{L}_{k,u}} \mathbf{x}_k(0,0)}^{\mathbf{x}_k(t_d, t_u)}, \quad (11)$$

where $\mathbf{x}_{k,d}(0)$, $\mathbf{x}_{k,u}(0)$, and $\mathbf{x}_k(0,0)$ are the initial conditions for the PDEs.

Using (11) and extending the solution to the multidimensional case, we propose the l -th layer of COSMOS as:

$$\mathbf{X}_k^l = \sigma \left(e^{-t_d \mathbf{L}_{k,d}} \mathbf{X}_{k,d}^{l-1} \Theta_{k,d}^l + e^{-t_u \mathbf{L}_{k,u}} \mathbf{X}_{k,u}^{l-1} \Theta_{k,u}^l + e^{-t_d \mathbf{L}_{k,d}} \mathbf{X}_k^{l-1} \Psi_{k,d}^l + e^{-t_u \mathbf{L}_{k,u}} \mathbf{X}_k^{l-1} \Psi_{k,u}^l \right), \quad (12)$$

where $\sigma(\cdot)$ is a nonlinearity, $\{\Theta_{k,d}^l, \Theta_{k,u}^l, \Psi_{k,d}^l, \Psi_{k,u}^l\}$ are learnable linear projections in $\mathbb{R}^{F_{l-1} \times F_l}$, and $\{\mathbf{X}_k^0, \mathbf{X}_{k,d}^0, \mathbf{X}_{k,u}^0\}$ are the initial conditions.

Remark 4.2. One possible approach to make our model more expressive is the aggregation of M learnable branches. Let $f_{k,l}^{(m)}(\mathbf{X}; t, \Theta, \Psi)$ be the m -th branch of layer l as the right-hand side of the COSMOS model in (12), where $\mathbf{X} = \{\mathbf{X}_k^0, \mathbf{X}_{k,d}^0, \mathbf{X}_{k,u}^0\}$, $t = \{t_d^{(m)}, t_u^{(m)}\}$, $\Theta = \{\Theta_{k,d}^{l,(m)}, \Theta_{k,u}^{l,(m)}\}$, and $\Psi = \{\Psi_{k,d}^{l,(m)}, \Psi_{k,u}^{l,(m)}\}$. The output for the l -th layer can be stated as:

$$\mathbf{X}_k^l = \text{AGG} \left(\left\{ f_{k,l}^{(m)}(\mathbf{X}; t, \Theta, \Psi) \right\}_{m=1}^M \right), \quad (13)$$

where $\text{AGG}(\cdot)$ is a well-defined aggregation function, *e.g.*, a multilayer perceptron.

4.3 Computational Complexity of COSMOS

For the efficient implementation of exponential Hodge filters, we benefit from the eigenvalue decomposition (EVD) of the Hodge Laplacians [13, 36]. Precisely, for a sample Laplacian $\mathbf{L} \in \mathbb{R}^{N \times N}$ with the eigenvalues $\lambda_0 = 0 \leq \lambda_1 \leq \dots \leq \lambda_{N-1}$, after performing EVD, $\mathbf{L} = \mathbf{V}\mathbf{\Lambda}\mathbf{V}^\top$, the exponential Laplacian filtering operation on input data $\mathbf{X} \in \mathbb{R}^{N \times F}$ and learnable weight matrix $\mathbf{W} \in \mathbb{R}^{F \times F'}$ can be implemented as:

$$e^{-t\mathbf{L}}\mathbf{X}\mathbf{W} \approx \mathbf{V}^{(K)} \left(\underbrace{[\tilde{\lambda}^{(K)} | \dots | \tilde{\lambda}^{(K)}]}_{\tilde{\mathbf{\Lambda}}} \odot (\mathbf{V}^{(K)\top} \mathbf{X}) \right) \mathbf{W}, \quad (14)$$

where

$$\tilde{\mathbf{\Lambda}} := e^{-t\boldsymbol{\lambda}^{(K)}} = (e^{-t\lambda_{N-1}}, \dots, e^{-t\lambda_{N-K}})^\top, \quad (15)$$

$\mathbf{V}^{(K)} \in \mathbb{R}^{N \times K}$ is built by choosing K most dominant eigenvalue-eigenvector pairs of \mathbf{L} , and \odot states the element-wise multiplication. As K gets closer to N , the estimation is more accurate. Using the implementation in (14), the computational complexity of the EVD decreases from $\mathcal{O}(N^3)$ to $\mathcal{O}(KN^2)$. Therefore, the computational complexity of calculating the Hodge-aware exponential Hodge filters in (11) can be reduced from $\mathcal{O}(|\mathcal{X}_k|^3)$ to $\mathcal{O}(|\mathcal{X}_k|^2 (K_k^{(d)} + K_k^{(u)} + K_k))$, where $K_k^{(d)}$, $K_k^{(u)}$, and K_k are the most dominant eigenvalue-eigenvector pairs of $\mathbf{L}_{k,d}$, $\mathbf{L}_{k,u}$, and \mathbf{L}_k , respectively.

4.4 Stability Analysis

Here, we study the robustness of our model against simplicial perturbations. We model these perturbations as structural inaccuracies in the incidence matrices, given by $\tilde{\mathbf{B}}_k = \mathbf{B}_k + \mathbf{E}_k$ and $\tilde{\mathbf{B}}_{k+1} = \mathbf{B}_{k+1} + \mathbf{E}_{k+1}$, where $\|\mathbf{E}_k\| \leq \epsilon_k$ and $\|\mathbf{E}_{k+1}\| \leq \epsilon_{k+1}$ represent the perturbation errors. Building upon these additive models, the perturbed Hodge operator is expressed as $\tilde{\mathbf{L}}_k = \tilde{\mathbf{L}}_{k,d} + \tilde{\mathbf{L}}_{k,u} = \tilde{\mathbf{B}}_k^\top \tilde{\mathbf{B}}_k + \tilde{\mathbf{B}}_{k+1}^\top \tilde{\mathbf{B}}_{k+1}$. The following theorem bounds the error between true and perturbed targets, *i.e.*, $\delta_{\mathbf{X}_k} := \|\tilde{\mathbf{X}}_k(t_d, t_u) - \mathbf{X}_k(t_d, t_u)\|$.

Theorem 4.3. *Given the additive simplicial perturbation models $\tilde{\mathbf{B}}_k = \mathbf{B}_k + \mathbf{E}_k$ and $\tilde{\mathbf{B}}_{k+1} = \mathbf{B}_{k+1} + \mathbf{E}_{k+1}$, where $\|\mathbf{E}_k\| \leq \epsilon_k$ and $\|\mathbf{E}_{k+1}\| \leq \epsilon_{k+1}$, the error between true and perturbed targets in (11) is bounded as:*

$$\delta_{\mathbf{X}_k} \leq t_d \delta_{k,d} e^{t_d \delta_{k,d}} (\|\mathbf{x}_{k,d}(0)\| + \|\mathbf{x}_k(0,0)\|) + t_u \delta_{k,u} e^{t_u \delta_{k,u}} (\|\mathbf{x}_{k,u}(0)\| + \|\mathbf{x}_k(0,0)\|), \quad (16)$$

where

$$\begin{aligned} \delta_{k,d} &:= 2\sqrt{\lambda_{\max}(\mathbf{L}_{k,d})\epsilon_k + \epsilon_k^2}, \\ \delta_{k,u} &:= 2\sqrt{\lambda_{\max}(\mathbf{L}_{k,u})\epsilon_{k+1} + \epsilon_{k+1}^2}. \end{aligned} \quad (17)$$

Theorem 4.3 shows how the robustness of the model is influenced by the maximum eigenvalues of $\mathbf{L}_{k,d}$ and $\mathbf{L}_{k,u}$, as well as by the Hodge receptive fields t_d and t_u . Furthermore, the error bounds of ϵ_k and ϵ_{k+1} play a critical role in determining $\delta_{k,d}$ and $\delta_{k,u}$, which ultimately control the stability. The following corollary simplifies Theorem 4.3 under the assumption of sufficiently small error bounds.

Corollary 4.4. *When the error bounds ϵ_k and ϵ_{k+1} are sufficiently small, the error between the true and perturbed targets is given by:*

$$\delta_{\mathbf{X}_k} = \mathcal{O}(\epsilon_k) + \mathcal{O}(\epsilon_{k+1}). \quad (18)$$

Corollary 4.4 demonstrates the stability of the proposed network against small simplicial perturbations.

5 Understanding Over-smoothing in SNNs

In this section, we first comprehensively analyze the over-smoothing problem in discrete SNNs. Next, we study over-smoothing in COSMOS highlighting the key differences with discrete SNNs. In both cases, we focus on the convergence of the Dirichlet energy to zero, which indicates that the simplicial signals have become constant, meaning no discriminative information remains.

5.1 Over-smoothing in Discrete SNNs

Based on the discrete SNN in (6) with $T_d = T_u = 1$ and Definition 3.1, the following theorem characterizes the over-smoothing properties of the discrete SNN.

Theorem 5.1. *In the discrete SNN in (6) and nonlinearity functions $\text{ReLU}(\cdot)$ or $\text{LeakyReLU}(\cdot)$, the Dirichlet energy of the simplicial signals at the $l + 1$ -th layer is bounded by the Dirichlet energy of the l -th layer and some structural and architectural characteristics as:*

$$E(\mathbf{X}_k^{l+1}) \leq s \tilde{\lambda}_{\max}^3 (E_{k-1}(\mathbf{X}_{k-1}^l) + E_{k+1}(\mathbf{X}_{k+1}^l)) + 2s \tilde{\lambda}_{\max}^{3.5} \|\mathbf{X}_k^l\| (\|\mathbf{X}_{k-1}^l\| + \|\mathbf{X}_{k+1}^l\|) + 2s \tilde{\lambda}_{\max}^2 E(\mathbf{X}_k^l), \quad (19)$$

where

$$\begin{aligned} \tilde{\lambda}_{\max} &:= \max_k \{\lambda_{\max}(\mathbf{L}_{k,d}), \lambda_{\max}(\mathbf{L}_{k,u})\}, \\ s &:= \sqrt{\max_{k,l} \left\{ \|\mathbf{W}_{k,d}^l\|, \|\mathbf{W}_{k,u}^l\| \right\}}. \end{aligned} \quad (20)$$

The upper bound in (19) consists of three terms, all of which can potentially converge to zero in the case of stacking several layers, *i.e.*, increasing l . In this way, under some practically justified conditions, the upper bound in (19) converges to zero, *i.e.*, the over-smoothing phenomenon, as described in the next corollary:

Corollary 5.2. *In (19), if $\tilde{\lambda}_{\max} < \min \left\{ s^{-\frac{1}{3}}, s^{-\frac{1}{3.5}}, s^{-\frac{1}{2}} \right\}$, then $\lim_{l \rightarrow \infty} E(\mathbf{X}_k^l) \rightarrow 0$.*

With the assumption in Corollary 5.2, we should modify $\tilde{\lambda}_{\max}$ to control the upper bound in (19). This involves modifying the structural properties of the simplicial complex. Therefore, preventing discrete SNNs from converging to the over-smoothing state is not straightforward.

5.2 Over-smoothing in COSMOS

The next theorem characterizes the counterpart of Theorem 5.1 in the continuous settings.

Theorem 5.3. *By considering the continuous Hodge learning framework in (12) and nonlinearity functions $\text{ReLU}(\cdot)$ or $\text{LeakyReLU}(\cdot)$, it holds:*

$$E(\mathbf{X}_k^{l+1}) \leq \tilde{\lambda}_{\max} e^{-2\varphi} (E(\mathbf{X}_{k-1}^l) + E_{k+1}(\mathbf{X}_{k+1}^l)) + 2s \tilde{\lambda}_{\max}^{1.5} \|\mathbf{X}_k^l\| (\|\mathbf{X}_{k-1}^l\| + \|\mathbf{X}_{k+1}^l\|) + 2s e^{-2\varphi} E(\mathbf{X}_k^l), \quad (21)$$

where

$$\varphi := \min_k \{t_d \lambda_{\min}(\mathbf{L}_{k,d}), t_u \lambda_{\min}(\mathbf{L}_{k,u})\}. \quad (22)$$

We observe that the two first terms in (21) tend to converge to zero as in (19) when stacking multiple layers. However, the third term might have a different behavior described in the following corollary.

Corollary 5.4. *The upper bound in (21) exponentially converges to zero when stacking multiple layers if:*

$$\ln s < \min \left(2\varphi, -\frac{2 \ln \lambda_{\max}}{3} \right). \quad (23)$$

Assuming $t_d = t_u = t$ in (11) and considering t as a hyperparameter, one heuristic to prevent over-smoothing in COSMOS is stated in the next proposition.

Proposition 5.5. *If $\ln s > 2\varphi$ (violating one of the conditions in (23)), then:*

$$t < \frac{\ln s}{\lambda_{\min}(\mathbf{L}_k)} + k_f(\mathbf{L}_k), \quad (24)$$

where $k_f(\mathbf{L}_k)$ is the finite condition number [37] of the k -simplex.

Table 1: Accuracy (%) results in trajectory prediction task on the synthetic and ocean drifts datasets.

Method	Synthetic \uparrow	Ocean Drifts \uparrow
SNN	65.5 \pm 2.4	52.5 \pm 6.0
PSNN	63.1 \pm 3.1	49.0 \pm 8.0
SCNN	67.7 \pm 1.7	53.0 \pm 7.8
Bunch	62.3 \pm 4.0	46.0 \pm 6.2
SCCNN	65.2 \pm 4.1	<u>54.5 \pm 7.9</u>
COSMOS	<u>65.9 \pm 4.4</u>	55.0 \pm 5.5

Table 2: MSE in the task of regression on partial deformable shapes on the Shrec-16 dataset.

Method	Small \downarrow	Full \downarrow
HSN	0.138 \pm 0.001	0.133 \pm 0.001
SCACMPS	0.137 \pm 0.011	0.432 \pm 0.001
SAN	0.052 \pm 0.011	0.075 \pm 0.002
SCCNN	<u>0.020 \pm 0.003</u>	0.063 \pm 0.003
COSMOS	0.010 \pm 0.004	0.027 \pm 0.007

Theorem 5.3 aligns with the main takeaways in the GNN literature [13, 38], where increasing the graph receptive field leads to an increase in the mixing rate of the node features, leading to a faster convergence to the over-smoothing state. We observe from Proposition 5.5 that decreasing the simplicial receptive field t can alleviate over-smoothing, which is a key difference from the discrete case discussed in Section 5.1. We experimentally validate this claim in Section 6. Besides stability and over-smoothing, we show the permutation equivariance property of COSMOS in Appendix K.

6 Experiments and Results

In this section, we evaluate COSMOS against state-of-the-art methods in applications of trajectory prediction and simplicial-based mesh regression. Then, we experimentally validate the theoretical claims in this paper.

6.1 Implementation Details

In certain cases, we use TopoModelX [20, 39, 40] to implement previous state-of-the-art methods. For access and processing real-world datasets, we employ Torch TopoNetX [40]. For the experiments on trajectory prediction, we use the aggregation of M branches discussed in Remark 4.2. Detailed hyperparameter configurations for both synthetic and real-world datasets are provided in the code in the supplementary material.

6.2 Real-world Applications

Trajectory prediction. Trajectory prediction involves forecasting paths within simplicial complexes. To evaluate the effectiveness of COSMOS, we assess its performance on two datasets: a synthetic simplicial complex and the ocean drifter dataset from [23, 41]. We compare COSMOS against several baseline models, including SNN [16], PSNN [23], SCNN [24], Bunch [28], and SCCNN [30, 31].

As shown in Table 1, COSMOS, SCCNN, and Bunch, which incorporate inter-simplicial couplings, do not outperform SCNN on the synthetic dataset. This is likely because the input data assigned to nodes and triangles is zero, as noted in [23], making inter-simplicial couplings ineffective. However, in the ocean drifter dataset, where higher-order information plays a more significant role, incorporating higher-order convolutions—as in COSMOS and SCCNN—improves the average accuracy.

It is important to note that trajectory prediction in this context involves identifying a candidate node within the neighborhood of the target node, a process influenced by node degree. Given that the average node degree is 5.24 in the synthetic dataset and 4.81 in the ocean drifter dataset, a random guess would achieve approximately 20% accuracy. The high standard deviations observed, particularly in the ocean drifter dataset, may be attributed to its limited size.

Regression on partial deformable shapes. The Shrec-16 benchmark [42] extends prior mesh classification datasets to meshes with missing parts. Using 76 near-isometric shapes from the TOSCA dataset [43], where each class has a

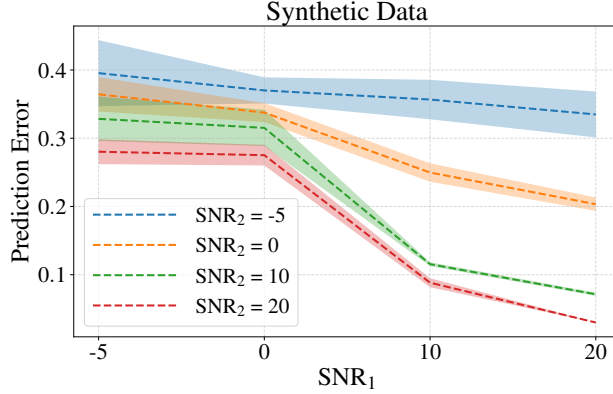


Figure 3: Stability analysis of the proposed method under varying signal-to-noise ratios (SNRs). The x-axis represents different values of SNR_1 , while the y-axis shows the corresponding prediction error. Each curve represents a different SNR_2 setting, with shaded regions indicating standard deviations.

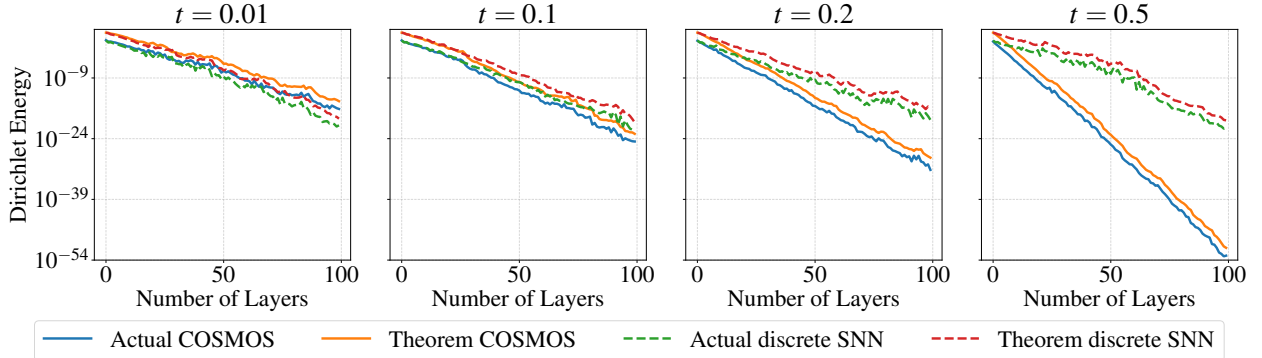


Figure 4: Over-smoothing results of discrete SNNs and COSMOS across different layer depths. Each subplot corresponds to a different parameter t in COSMOS, showing the evolution of the Dirichlet energy as a function of the number of layers.

full template in a neutral pose for evaluation. To increase complexity, all shapes were sampled to 10K vertices before introducing missing parts in two ways: regular cuts, where template shapes were sliced at six orientations, producing 320 partial shapes, and irregular holes, where surface erosion was applied based on area budgets (40%, 70%, and 90%), yielding 279 shapes. This results in a dataset of 599 shapes across eight classes (humans and animals), with varying missing areas (10%–60%). The dataset is divided into a training set (199 shapes) and a test set (400 shapes). The main task here is to regress the correct mesh class under missing parts.

We compare COSMOS against state-of-the-art methods, including HSN [44], SCACMPS [20], SAN [10], and SCCNN [30], on two versions of the Shrec-16 dataset: *small* and *full*. As shown in Table 2, COSMOS achieves the lowest mean square error (MSE) in mesh regression on both dataset versions, outperforming all baselines. Notably, its superior performance across both small and full versions highlights its adaptability to different amounts of training data, showing strong performance even with limited data.

6.3 Stability Analysis

We generate simplicial complexes of dimension 2, following the approach in [23]: (i) we uniformly sample $N = 30$ random points from the unit square and construct the Delaunay triangulation, and (ii) we remove triangles contained within predefined disk regions. For our experiment, we use the generative model in (11) with $k = 1$, $t_d = 1$, and $t_u = 2$, generating $\{\mathbf{X}_k^0 \in \mathbb{R}^{|\mathcal{X}_k| \times 1}\}_{k=0}^2$ from normal probability distributions. After extracting the incidence matrices \mathbf{B}_1 and \mathbf{B}_2 , we introduce noise by varying their respective signal-to-noise ratios (SNRs) in $\{-5, 0, 10, 20\}$ dB. For each setting, we train COSMOS and evaluate its prediction performance, averaging results over 30 random realizations. Figure 3 presents the results, including standard deviations. These results confirm that the model’s overall stability arises from the stability at each order k , validating the theoretical findings of Theorem 4.3.

6.4 Over-smoothing Analysis

The goals of this section are twofold: (i) to validate Theorems 5.1 and 5.3, and (ii) to study the behavior of discrete SNNs in (6) and COSMOS in (12) when facing over-smoothing. For the discrete SNN, we consider $T_d = T_u = 1$ ($i = 1$) in (6). For COSMOS in (12), we explore different scenarios by adjusting the receptive fields $t_d = t_u = t$ where $t \in \{10^{-2}, 10^{-1}, 0.2, 0.5\}$. In both cases, the corresponding linear projections—with hidden units $F_{l-1} = F_l = 4$ —are generated from normal distributions.

Figure 4 shows the left-hand side (LHS) and right-hand side (RHS) of Theorems 5.1 and 5.3 averaged over 50 random realizations with number of layers varying from 1 to 100. These results validate Theorems 5.1 and 5.3, confirming that the LHSs are upper bounded by the RHSs. We also observe that adjusting t in COSMOS provides control over the over-smoothing rate, *i.e.*, how quickly the output of the SNN converges to zero Dirichlet energy. Specifically, setting $t = 10^{-2}$ results in a slower over-smoothing rate in COSMOS compared to the discrete SNN. In contrast, increasing t leads to a faster over-smoothing rate in COSMOS than in the discrete SNN. This shows that variations in the continuous receptive fields in (12) directly influence the rate of convergence to the over-smoothing state. Additional analysis has been provided in the Appendix (Section I).

Note that decreasing t too much can negatively impact the topology of the simplicial complex, potentially leading to issues like over-squashing of information [45], which could degrade performance. A thorough analysis of this variation is beyond the scope of the current paper and will be explored in future work.

7 Conclusion

In this paper, we have introduced COSMOS, a novel Hodge-aware model for filtering simplicial signals that addresses the limitations of discrete SNNs by incorporating dynamic receptive fields. We provided rigorous theoretical analyses of the stability and over-smoothing behavior of our model, offering new insights into its performance. Through extensive experiments, we validated our theoretical findings, demonstrating that COSMOS is not only stable but also allows for effective control over the over-smoothing rate through its continuous receptive fields. Our experimental results highlight the superiority of COSMOS over existing state-of-the-art SNNs, particularly in challenging trajectory prediction and regression of partial shape tasks. This is especially evident in complex and noisy datasets, such as the ocean drifter and Shrec-16 datasets, where our method consistently outperforms previous models.

Acknowledgments

This research was supported by DATAIA Convergence Institute as part of the «Programme d’Investissement d’Avenir», (ANR-17-CONV-0003) operated by the center Hi! PARIS. This work was also partially supported by the EuroTech Universities Alliance, and the ANR French National Research Agency under the JCJC projects DeSNAP (ANR-24-CE23-1895-01), and GraphIA (ANR-20-CE23-0009-01).

References

- [1] Z. Wu, S. Pan, F. Chen, G. Long, C. Zhang, and S. Y. Philip, “A comprehensive survey on graph neural networks,” *IEEE Transactions on Neural Networks and Learning Systems*, vol. 32, no. 1, pp. 4–24, 2020.
- [2] M. Defferrard, X. Bresson, and P. Vandergheynst, “Convolutional neural networks on graphs with fast localized spectral filtering,” in *Advances in Neural Information Processing Systems*, vol. 29, 2016.
- [3] T. N. Kipf and M. Welling, “Semi-supervised classification with graph convolutional networks,” in *International Conference on Learning Representations*, 2017.
- [4] P. Veličković, G. Cucurull, A. Casanova, A. Romero, P. Liò, and Y. Bengio, “Graph attention networks,” in *International Conference on Learning Representations*, 2018.
- [5] W. Uwents, G. Monfardini, H. Blockeel, M. Gori, and F. Scarselli, “Neural networks for relational learning: An experimental comparison,” *Machine Learning*, vol. 82, no. 3, pp. 315–349, 2011.
- [6] P. Gainza, F. Sverrisson, F. Monti, E. Rodola, D. Boscaini, M. M. Bronstein, and B. E. Correia, “Deciphering interaction fingerprints from protein molecular surfaces using geometric deep learning,” *Nature Methods*, 2020.
- [7] A. A. Duval, V. Schmidt, A. Hernández-García, S. Miret, F. D. Malliaros, Y. Bengio, and D. Rolnick, “FAENet: Frame averaging equivariant GNN for materials modeling,” in *International Conference on Machine Learning*, 2023.

- [8] G. Li *et al.*, “DeepGCNs: Can GCNs go as deep as CNNs?,” in *IEEE/CVF International Conference on Computer Vision*, 2019.
- [9] J. H. Giraldo, S. Javed, and T. Bouwmans, “Graph moving object segmentation,” *IEEE Transactions on Pattern Analysis and Machine Intelligence*, vol. 44, no. 5, pp. 2485–2503, 2020.
- [10] L. Giusti, C. Battiloro, P. Di Lorenzo, S. Sardellitti, and S. Barbarossa, “Simplicial attention neural networks,” *arXiv preprint arXiv:2203.07485*, 2022.
- [11] A. Han, D. Shi, L. Lin, and J. Gao, “From continuous dynamics to graph neural networks: Neural diffusion and beyond,” *Transactions on Machine Learning Research*, 2024.
- [12] Y. Song, Q. Kang, S. Wang, K. Zhao, and W. P. Tay, “On the robustness of graph neural diffusion to topology perturbations,” in *Advances in Neural Information Processing Systems*, 2022.
- [13] A. Einizade, F. Malliaros, and J. H. Giraldo, “Continuous product graph neural networks,” in *Advances in Neural Information Processing Systems*, 2024.
- [14] S. Barbarossa and S. Sardellitti, “Topological signal processing over simplicial complexes,” *IEEE Transactions on Signal Processing*, vol. 68, pp. 2992–3007, 2020.
- [15] E. Isufi, G. Leus, B. Beferull-Lozano, S. Barbarossa, and P. Di Lorenzo, “Topological signal processing and learning: Recent advances and future challenges,” *arXiv preprint arXiv:2412.01576*, 2024.
- [16] S. Ebli, M. Defferrard, and G. Spreemann, “Simplicial neural networks,” in *Advances in Neural Information Processing Systems - Workshops*, 2020.
- [17] H. Wu, A. Yip, J. Long, J. Zhang, and M. K. Ng, “Simplicial complex neural networks,” *IEEE Transactions on Pattern Analysis and Machine Intelligence*, 2023.
- [18] C. Bodnar, F. Frasca, Y. Wang, N. Otter, G. F. Montufar, P. Lio, and M. Bronstein, “Weisfeiler and Lehman go topological: Message passing simplicial networks,” in *International Conference on Machine Learning*, 2021.
- [19] T. Papamarkou, T. Birdal, M. M. Bronstein, G. E. Carlsson, J. Curry, Y. Gao, M. Hajj, R. Kwitt, P. Lio, P. D. Lorenzo, V. Maroulas, N. Miolane, F. Nasrin, K. N. Ramamurthy, B. Rieck, S. Scardapane, M. T. Schaub, P. Veličković, B. Wang, Y. Wang, G. Wei, and G. Zamzmi, “Position: Topological deep learning is the new frontier for relational learning,” in *International Conference on Machine Learning*, 2024.
- [20] M. Papillon, S. Sanborn, M. Hajj, and N. Miolane, “Architectures of topological deep learning: A survey of message-passing topological neural networks,” *arXiv preprint arXiv:2304.10031*, 2023.
- [21] C. W. J. Goh, C. Bodnar, and P. Lio, “Simplicial attention networks,” in *International Conference on Learning Representations - Workshop*, 2022.
- [22] T. M. Roddenberry and S. Segarra, “HodgeNet: Graph neural networks for edge data,” in *Asilomar Conference on Signals, Systems, and Computers*, 2019.
- [23] T. M. Roddenberry, N. Glaze, and S. Segarra, “Principled simplicial neural networks for trajectory prediction,” in *International Conference on Machine Learning*, 2021.
- [24] M. Yang, E. Isufi, and G. Leus, “Simplicial convolutional neural networks,” in *IEEE International Conference on Acoustics, Speech and Signal Processing*, 2022.
- [25] A. D. Keros, V. Nanda, and K. Subr, “Dist2Cycle: A simplicial neural network for homology localization,” in *AAAI Conference on Artificial Intelligence*, 2022.
- [26] Y. Chen, Y. R. Gel, and H. V. Poor, “BScNets: Block simplicial complex neural networks,” in *AAAI Conference on Artificial Intelligence*, 2022.
- [27] S. H. Lee, F. Ji, and W. P. Tay, “SGAT: Simplicial graph attention network,” in *International Joint Conference on Artificial Intelligence*, 2022.
- [28] E. Bunch, Q. You, G. Fung, and V. Singh, “Simplicial 2-complex convolutional neural networks,” in *Advances in Neural Information Processing Systems - Workshops*, 2020.
- [29] R. Yang, F. Sala, and P. Bogdan, “Efficient representation learning for higher-order data with simplicial complexes,” in *Learning on Graphs Conference*, 2022.
- [30] M. Yang and E. Isufi, “Convolutional learning on simplicial complexes,” *arXiv preprint arXiv:2301.11163*, 2023.
- [31] M. Yang and E. Isufi, “Hodge-aware learning on simplicial complexes,” 2023.
- [32] M. Hajj, G. Zamzmi, T. Papamarkou, V. Maroulas, and X. Cai, “Simplicial complex representation learning,” in *International Conference on Learning Representations - Workshops*, 2021.

- [33] K. Xu, W. Hu, J. Leskovec, and S. Jegelka, “How powerful are graph neural networks?,” in *International Conference on Learning Representations*, 2019.
- [34] E. Isufi and M. Yang, “Convolutional filtering in simplicial complexes,” in *IEEE International Conference on Acoustics, Speech and Signal Processing*, 2022.
- [35] A. Ortega *et al.*, “Graph signal processing: Overview, challenges, and applications,” *Proceedings of the IEEE*, vol. 106, no. 5, pp. 808–828, 2018.
- [36] M. Behmanesh, M. Krahn, and M. Ovsjanikov, “TIDE: Time derivative diffusion for deep learning on graphs,” in *International Conference on Machine Learning*, 2023.
- [37] D. A. Spielman, “Algorithms, graph theory, and linear equations in laplacian matrices,” in *International Congress of Mathematicians*, 2010.
- [38] K. Oono and T. Suzuki, “Graph neural networks exponentially lose expressive power for node classification,” in *International Conference on Learning Representations*, 2020.
- [39] M. Hajij, G. Zamzmi, T. Papamarkou, N. Miolane, A. Guzmán-Sáenz, K. N. Ramamurthy, T. Birdal, T. K. Dey, S. Mukherjee, S. N. Samaga, N. Livesay, R. Walters, P. Rosen, and M. T. Schaub, “Topological deep learning: Going beyond graph data,” 2023.
- [40] M. Hajij, M. Papillon, F. Frantzen, J. Agerberg, I. AlJabea, R. Ballester, C. Battiloro, G. Bernárdez, T. Birdal, A. Brent, *et al.*, “Topox: a suite of python packages for machine learning on topological domains,” *Journal of Machine Learning Research*, vol. 25, no. 374, pp. 1–8, 2024.
- [41] M. T. Schaub, A. R. Benson, P. Horn, G. Lippner, and A. Jadbabaie, “Random walks on simplicial complexes and the normalized Hodge 1-laplacian,” *SIAM Review*, vol. 62, no. 2, pp. 353–391, 2020.
- [42] L. Cosmo, E. Rodola, M. M. Bronstein, A. Torsello, D. Cremers, Y. Sahillioğlu, *et al.*, “Shrec’16: Partial matching of deformable shapes,” in *Eurographics Workshop on 3D Object Retrieval*, 2016.
- [43] A. M. Bronstein, M. M. Bronstein, and R. Kimmel, *Numerical geometry of non-rigid shapes*. Springer Science & Business Media, 2008.
- [44] M. Hajij, K. N. Ramamurthy, A. Guzmán-Sáenz, and G. Za, “High skip networks: A higher order generalization of skip connections,” *International Conference on Learning Representations - Workshops*, 2022.
- [45] J. H. Giraldo, K. Skianis, T. Bouwmans, and F. D. Malliaros, “On the trade-off between over-smoothing and over-squashing in deep graph neural networks,” in *ACM International Conference on Information and Knowledge Management*, 2023.
- [46] C. Van Loan, “The sensitivity of the matrix exponential,” *SIAM Journal on Numerical Analysis*, vol. 14, no. 6, pp. 971–981, 1977.
- [47] C. Cai and Y. Wang, “A note on over-smoothing for graph neural networks,” *arXiv preprint arXiv:2006.13318*, 2020.

A Proof of Proposition 4.1

Proof. By considering the proposed solution in (11) as follows:

$$\mathbf{x}'_k(t_d, t_u) = \overbrace{e^{-t_d \mathbf{L}_{k,d}} \mathbf{x}_{k,d}(0)}^{\mathbf{x}_{k,d}(t_d)} + \overbrace{e^{-t_u \mathbf{L}_{k,u}} \mathbf{x}_{k,u}(0)}^{\mathbf{x}_{k,u}(t_u)} + \overbrace{e^{-t_d \mathbf{L}_{k,d}} \mathbf{x}_k(0,0) + e^{-t_u \mathbf{L}_{k,u}} \mathbf{x}_k(0,0)}^{\mathbf{x}_k(t_d, t_u)}, \quad (25)$$

the simplified generative PDE of this formulation can be expressed as:

$$\begin{aligned} \frac{\partial \mathbf{x}_{k,d}(t_d)}{\partial t_d} &= -\mathbf{L}_{k,d} e^{-t_d \mathbf{L}_{k,d}} \mathbf{x}_{k,d}(0) = -\mathbf{L}_{k,d} \mathbf{x}_{k,d}(t_d), \\ \frac{\partial \mathbf{x}_{k,u}(t_u)}{\partial t_u} &= -\mathbf{L}_{k,u} e^{-t_u \mathbf{L}_{k,u}} \mathbf{x}_{k,u}(0) = -\mathbf{L}_{k,u} \mathbf{x}_{k,u}(t_u), \\ \mathbf{x}_k(t_d, t_u) &= e^{-t_d \mathbf{L}_{k,d}} \mathbf{x}_k(0,0) + e^{-t_u \mathbf{L}_{k,u}} \mathbf{x}_k(0,0), \\ \rightarrow \lim_{t_d \rightarrow \infty} \mathbf{x}_k(t_d, t_u) &= e^{-t_u \mathbf{L}_{k,u}} \mathbf{x}_k(0,0), \quad \lim_{t_u \rightarrow \infty} \mathbf{x}_k(t_d, t_u) = e^{-t_d \mathbf{L}_{k,d}} \mathbf{x}_k(0,0), \\ \rightarrow \frac{\partial \mathbf{x}_k(t_d, t_u)}{\partial t_d} &= -\mathbf{L}_{k,d} e^{-t_d \mathbf{L}_{k,d}} \mathbf{x}_k(0,0), \quad \frac{\partial \mathbf{x}_k(t_d, t_u)}{\partial t_u} = -\mathbf{L}_{k,u} e^{-t_u \mathbf{L}_{k,u}} \mathbf{x}_k(0,0). \end{aligned} \quad (26)$$

Therefore,

$$\frac{\partial \mathbf{x}_k(t_d, t_u)}{\partial t_d} + \frac{\partial \mathbf{x}_k(t_d, t_u)}{\partial t_u} = -\mathbf{L}_{k,d} \overbrace{\lim_{t_d \rightarrow \infty} \mathbf{x}_k(t_d, t_u)}^{\mathbf{x}_k(t_d, \infty)} - \mathbf{L}_{k,u} \overbrace{\lim_{t_d \rightarrow \infty} \mathbf{x}_k(t_d, t_u)}^{\mathbf{x}_k(\infty, t_u)}, \quad (27)$$

which concludes the proof. \square

B Proof of Theorem 4.3

Proof. Using the additive perturbation models and the triangular inequality principle, one can write:

$$\begin{aligned} \|\tilde{\mathbf{L}}_{k,d} - \mathbf{L}_{k,d}\| &\leq 2\|\mathbf{B}_k\| \|\mathbf{E}_k\| + \|\mathbf{E}_k^\top \mathbf{E}_k\| \leq 2\epsilon_k \sqrt{\lambda_{\max}(\mathbf{L}_{k,d})} + \epsilon_k^2 \stackrel{\text{if } \epsilon_k \text{ is small}}{\approx} \mathcal{O}(\epsilon_k), \\ \|\tilde{\mathbf{L}}_{k,u} - \mathbf{L}_{k,u}\| &\leq 2\|\mathbf{B}_{k+1}\| \|\mathbf{E}_{k+1}\| + \|\mathbf{E}_{k+1}^\top \mathbf{E}_{k+1}\| \leq 2\epsilon_{k+1} \sqrt{\lambda_{\max}(\mathbf{L}_{k,u})} + \epsilon_{k+1}^2 \stackrel{\text{if } \epsilon_{k+1} \text{ is small}}{\approx} \mathcal{O}(\epsilon_{k+1}). \end{aligned} \quad (28)$$

Then, by the definitions $\delta_{k,d} := 2\epsilon_k \sqrt{\lambda_{\max}(\mathbf{L}_{k,d})} + \epsilon_k^2$ and $\delta_{k,u} := 2\epsilon_{k+1} \sqrt{\lambda_{\max}(\mathbf{L}_{k,u})} + \epsilon_{k+1}^2$, the bound on the exponential Hodge filters can be obtained as:

$$\begin{aligned} \|e^{-t_d \tilde{\mathbf{L}}_{k,d}} - e^{-t_d \mathbf{L}_{k,d}}\| &\leq t_d \overbrace{\|\tilde{\mathbf{L}}_{k,d} - \mathbf{L}_{k,d}\|}^{\delta_{k,d}} \overbrace{\|e^{-t_d \mathbf{L}_{k,d}}\|}^{e^{-t_d(0)}=1} e^{\|t_d(\tilde{\mathbf{L}}_{k,d} - \mathbf{L}_{k,d})\|} \leq t_d \delta_{k,d} e^{t_d \delta_{k,d}}, \\ \|e^{-t_u \tilde{\mathbf{L}}_{k,u}} - e^{-t_u \mathbf{L}_{k,u}}\| &\leq t_u \overbrace{\|\tilde{\mathbf{L}}_{k,u} - \mathbf{L}_{k,u}\|}^{\delta_{k,u}} \overbrace{\|e^{-t_u \mathbf{L}_{k,u}}\|}^{e^{-t_u(0)}=1} e^{\|t_u(\tilde{\mathbf{L}}_{k,u} - \mathbf{L}_{k,u})\|} \leq t_u \delta_{k,u} e^{t_u \delta_{k,u}}. \end{aligned} \quad (29)$$

Next, by considering the solution in (11), the perturbation bound can be expressed as:

$$\begin{aligned} \|\tilde{\mathbf{x}}_k(t_d, t_u) - \mathbf{x}_k(t_d, t_u)\| &\leq \|e^{-t_d \tilde{\mathbf{L}}_{k,d}} - e^{-t_d \mathbf{L}_{k,d}}\| \|\mathbf{x}_{k,d}(0)\| + \|e^{-t_u \tilde{\mathbf{L}}_{k,u}} - e^{-t_u \mathbf{L}_{k,u}}\| \|\mathbf{x}_{k,u}(0)\| \\ &\quad + (\|e^{-t_d \tilde{\mathbf{L}}_{k,d}} - e^{-t_d \mathbf{L}_{k,d}}\| + \|e^{-t_u \tilde{\mathbf{L}}_{k,u}} - e^{-t_u \mathbf{L}_{k,u}}\|) \|\mathbf{x}_k(0,0)\| \\ &\leq t_d \delta_{k,d} e^{t_d \delta_{k,d}} (\|\mathbf{x}_{k,d}(0)\| + \|\mathbf{x}_k(0,0)\|) + t_u \delta_{k,u} e^{t_u \delta_{k,u}} (\|\mathbf{x}_{k,u}(0)\| + \|\mathbf{x}_k(0,0)\|). \end{aligned} \quad (30)$$

\square

C Proof of Corollary 4.4

Proof. Based on the proof stated in Appendix B, we can bound $\|\tilde{\mathbf{L}}_k - \mathbf{L}_k\|$ as:

$$\begin{aligned} \|\tilde{\mathbf{L}}_k - \mathbf{L}_k\| &\leq \|\tilde{\mathbf{L}}_{k,d} - \mathbf{L}_{k,d}\| + \|\tilde{\mathbf{L}}_{k,u} - \mathbf{L}_{k,u}\| \leq 2\|\mathbf{B}_k\| \|\mathbf{E}_k\| + \|\mathbf{E}_k^\top \mathbf{E}_k\| + 2\|\mathbf{B}_{k+1}\| \|\mathbf{E}_{k+1}\| + \|\mathbf{E}_{k+1}^\top \mathbf{E}_{k+1}\| \\ &\leq 2\epsilon_k \sqrt{\lambda_{\max}(\mathbf{L}_{k,d})} + \epsilon_k^2 + 2\epsilon_{k+1} \sqrt{\lambda_{\max}(\mathbf{L}_{k,u})} + \epsilon_{k+1}^2 \\ &\stackrel{\text{if } \epsilon_k \text{ and } \epsilon_{k+1} \text{ are small}}{\approx} \mathcal{O}(\epsilon_k) + \mathcal{O}(\epsilon_{k+1}). \end{aligned} \quad (31)$$

Using this direction, it can be easily seen that:

$$\begin{aligned}\|\tilde{\mathbf{L}}_{k,d} - \mathbf{L}_{k,d}\| &\leq 2\|\mathbf{B}_k\| \|\mathbf{E}_k\| + \|\mathbf{E}_k^\top \mathbf{E}_k\| \leq 2\epsilon_k \sqrt{\lambda_{\max}(\mathbf{L}_{k,d})} + \epsilon_k^2 \stackrel{\text{if } \epsilon_k \text{ is small}}{\approx} \mathcal{O}(\epsilon_k) \\ \|\tilde{\mathbf{L}}_{k,u} - \mathbf{L}_{k,u}\| &\leq 2\|\mathbf{B}_{k+1}\| \|\mathbf{E}_{k+1}\| + \|\mathbf{E}_{k+1}^\top \mathbf{E}_{k+1}\| \leq 2\epsilon_{k+1} \sqrt{\lambda_{\max}(\mathbf{L}_{k,u})} + \epsilon_{k+1}^2 \stackrel{\text{if } \epsilon_{k+1} \text{ is small}}{\approx} \mathcal{O}(\epsilon_{k+1}).\end{aligned}\quad (32)$$

Now, for a sample Laplacian \mathbf{L} with $\|\tilde{\mathbf{L}} - \mathbf{L}\| = \mathcal{O}(\epsilon)$, one can write:

$$\|e^{-t\tilde{\mathbf{L}}} - e^{-t\mathbf{L}}\| \leq t\|\tilde{\mathbf{L}} - \mathbf{L}\| \|e^{-t\mathbf{L}}\| e^{t\|\tilde{\mathbf{L}} - \mathbf{L}\|} = \mathcal{O}(\epsilon t e^{-\rho t}) = \mathcal{O}(\epsilon), \quad (33)$$

for a positive constant ρ [46]. Therefore, by adapting (33), one can write:

$$\begin{aligned}\|e^{-t_d \tilde{\mathbf{L}}_{k,d}} - e^{-t_d \mathbf{L}_{k,d}}\| &\leq t_d \|\tilde{\mathbf{L}}_{k,d} - \mathbf{L}_{k,d}\| \|e^{-t_d \mathbf{L}_{k,d}}\| e^{t_d \|\tilde{\mathbf{L}}_{k,d} - \mathbf{L}_{k,d}\|} = \mathcal{O}(\epsilon_k t_d e^{-\rho_d t_d}) = \mathcal{O}(\epsilon_k), \\ \|e^{-t_u \tilde{\mathbf{L}}_{k,u}} - e^{-t_u \mathbf{L}_{k,u}}\| &\leq t_u \|\tilde{\mathbf{L}}_{k,u} - \mathbf{L}_{k,u}\| \|e^{-t_u \mathbf{L}_{k,u}}\| e^{t_u \|\tilde{\mathbf{L}}_{k,u} - \mathbf{L}_{k,u}\|} = \mathcal{O}(\epsilon_{k+1} t_u e^{-\rho_u t_u}) = \mathcal{O}(\epsilon_{k+1}).\end{aligned}\quad (34)$$

By considering (30) and (34), the proof is completed. \square

D Proof of Theorem 5.1

Proof. First, by stating the Dirichlet with $E(\cdot)$, we need the following lemmas from [47]:

Lemma D.1. (Lemma 3.2 in [47]). $E(\mathbf{X}\mathbf{W}) \leq \|\mathbf{W}^\top\|_2^2 E(\mathbf{X})$.

Lemma D.2. (Lemma 3.3 in [47]). For ReLU and Leaky-ReLU nonlinearities $E(\sigma(\mathbf{X})) \leq E(\mathbf{X})$.

Then,

$$\begin{aligned}E(\mathbf{X}_k^{l+1}) &= \text{tr}(\mathbf{X}_k^{l+1 \top} \mathbf{L}_{k,d} \mathbf{X}_k^{l+1}) + \text{tr}(\mathbf{X}_k^{l+1 \top} \mathbf{L}_{k,u} \mathbf{X}_k^{l+1}) \\ &\leq s\lambda_{\max}^2(\mathbf{L}_{k,d}) E(\mathbf{X}_{k,d}^l) + 2s\lambda_{\max}^3(\mathbf{L}_{k,d}) \|\mathbf{X}_{k,d}^l\|_2^2 + s\lambda_{\max}^2(\mathbf{L}_{k,d}) E(\mathbf{X}_k^l) \\ &\quad + s\lambda_{\max}^2(\mathbf{L}_{k,u}) E(\mathbf{X}_{k,u}^l) + 2s\lambda_{\max}^3(\mathbf{L}_{k,u}) \|\mathbf{X}_{k,u}^l\|_2^2 + s\lambda_{\max}^2(\mathbf{L}_{k,u}) E(\mathbf{X}_k^l) \\ &\leq s\lambda_{\max}^2(\mathbf{L}_{k,d}) \lambda_{\max}(\mathbf{L}_{k-1,u}) E_{k-1,u}(\mathbf{X}_{k-1}^l) + 2s\lambda_{\max}^{3.5}(\mathbf{L}_{k,d}) \|\mathbf{X}_{k-1}^l\|_2^2 + s\lambda_{\max}^2(\mathbf{L}_{k,d}) E(\mathbf{X}_k^l) \\ &\quad + s\lambda_{\max}^2(\mathbf{L}_{k,u}) \lambda_{\max}(\mathbf{L}_{k+1,d}) E_{k+1,d}(\mathbf{X}_{k+1}^l) + 2s\lambda_{\max}^{3.5}(\mathbf{L}_{k,u}) \|\mathbf{X}_{k+1}^l\|_2^2 + s\lambda_{\max}^2(\mathbf{L}_{k,u}) E(\mathbf{X}_k^l) \leq \\ &s\tilde{\lambda}_{\max}^3 E_{k-1,u}(\mathbf{X}_{k-1}^l) + 2s\tilde{\lambda}_{\max}^{3.5} \|\mathbf{X}_{k-1}^l\|_2^2 + s\tilde{\lambda}_{\max}^2 E(\mathbf{X}_k^l) + s\tilde{\lambda}_{\max}^3 E_{k+1,d}(\mathbf{X}_{k+1}^l) + 2s\tilde{\lambda}_{\max}^{3.5} \|\mathbf{X}_{k+1}^l\|_2^2 + s\tilde{\lambda}_{\max}^2 E(\mathbf{X}_k^l).\end{aligned}\quad (35)$$

\square

E Proof of Corollary 5.2

Proof. Using the results of Theorem 5.1, if the constraints of $s\tilde{\lambda}_{\max}^3 < 1$, $s\tilde{\lambda}_{\max}^{3.5} < 1$, and $s\tilde{\lambda}_{\max}^2 < 1$ are simultaneously satisfied, by stacking layers, their multiplications converge to zero making the RHS in Theorem 5.1 converge to zero as well. Holding the mentioned conditions together completes the proof. \square

F Proof of Theorem 5.3

Proof. First, consider that $E(\mathbf{x})$ can be stated by $\tilde{\mathbf{x}}$, i.e., the Graph Fourier Transform (GFT) [35] of \mathbf{x} (where $\{\lambda_i\}_{i=1}^N$ eigenvalues of the Laplacian $\hat{\mathbf{L}}$), as follows [47]:

$$E(\mathbf{x}) = \mathbf{x}^\top \hat{\mathbf{L}} \mathbf{x} = \sum_{i=1}^N \lambda_i \tilde{x}_i^2. \quad (36)$$

Next, taking λ as the smallest nonzero eigenvalue of the Laplacian $\hat{\mathbf{L}}$, the following lemma describes the behavior of a heat kernel in the most basic scenario of over-smoothing.

Lemma F.1. We have:

$$E(e^{-\hat{\mathbf{L}} \mathbf{x}}) \leq e^{-2\lambda} E(\mathbf{x}). \quad (37)$$

Proof. By showing the EVD of $\hat{\mathbf{L}} = \mathbf{V}\mathbf{\Lambda}\mathbf{V}^\top$ and $e^{-\hat{\mathbf{L}}} = \mathbf{V}e^{-\mathbf{\Lambda}}\mathbf{V}^\top$, we have:

$$\begin{aligned} & E(e^{-\hat{\mathbf{L}}}\mathbf{x}) \\ &= \mathbf{x}^\top \underbrace{\mathbf{V}e^{-\mathbf{\Lambda}}\mathbf{V}^\top}_{e^{-\hat{\mathbf{L}}}} \underbrace{\mathbf{V}\mathbf{\Lambda}\mathbf{V}^\top}_{\hat{\mathbf{L}}} \underbrace{\mathbf{V}e^{-\mathbf{\Lambda}}\mathbf{V}^\top}_{e^{-\hat{\mathbf{L}}}} \mathbf{x} = \sum_{i=1}^N \lambda_i \tilde{x}_i^2 e^{-2\lambda_i} \leq e^{-2\lambda} \left(\sum_{i=1}^N \lambda_i \tilde{x}_i^2 \right) = e^{-2\lambda} E(\mathbf{x}). \end{aligned} \quad (38)$$

Note that we excluded the zero eigenvalues because they do not engage in the calculation of Dirichlet energy. \square

Then, based on Lemmas D.1, D.2, and F.1, we can write:

$$\begin{aligned} E(\mathbf{X}_k^{l+1}) &= \text{tr}(\mathbf{X}_k^{l+1\top} \mathbf{L}_{k,d} \mathbf{X}_k^{l+1}) + \text{tr}(\mathbf{X}_k^{l+1\top} \mathbf{L}_{k,u} \mathbf{X}_k^{l+1}) \\ &= \underbrace{\text{tr}(\mathbf{W}_{k,d}^{l\top} \mathbf{X}_{k,d}^l e^{-t'_d \mathbf{L}_{k,d}} \mathbf{L}_{k,d} e^{-t'_d \mathbf{L}_{k,d}} \mathbf{X}_{k,d}^l \mathbf{W}_{k,d}^l)}_{\text{tr}(\mathbf{X}_{k,d}^{l\top} e^{-t'_d \mathbf{L}_{k,d}} \mathbf{L}_{k,d} e^{-t'_d \mathbf{L}_{k,d}} \mathbf{X}_{k,d}^l \mathbf{W}_{k,d}^l)} + 2 \underbrace{\text{tr}(\mathbf{W}_{k,d}^{l\top} \mathbf{X}_{k,d}^l e^{-t'_d \mathbf{L}_{k,d}} \mathbf{L}_{k,d} e^{-t_d \mathbf{L}_{k,d}} \mathbf{X}_k^l \mathbf{W}_{k,d}^l)}_{\text{tr}(\mathbf{X}_{k,d}^{l\top} e^{-t'_d \mathbf{L}_{k,d}} \mathbf{L}_{k,d} e^{-t_d \mathbf{L}_{k,d}} \mathbf{X}_k^l \mathbf{W}_{k,d}^l)} \\ &+ 2 \underbrace{\text{tr}(\mathbf{W}_{k,u}^{l\top} \mathbf{X}_{k,u}^l e^{-t'_u \mathbf{L}_{k,u}} \mathbf{L}_{k,u} e^{-t'_u \mathbf{L}_{k,u}} \mathbf{X}_{k,u}^l \mathbf{W}_{k,u}^l)}_{\text{tr}(\mathbf{X}_{k,u}^{l\top} e^{-t'_u \mathbf{L}_{k,u}} \mathbf{L}_{k,u} e^{-t'_u \mathbf{L}_{k,u}} \mathbf{X}_{k,u}^l \mathbf{W}_{k,u}^l)} + 2 \underbrace{\text{tr}(\mathbf{W}_{k,u}^{l\top} \mathbf{X}_{k,u}^l e^{-t'_u \mathbf{L}_{k,u}} \mathbf{L}_{k,u} e^{-t_u \mathbf{L}_{k,u}} \mathbf{X}_k^l \mathbf{W}_{k,u}^l)}_{\text{tr}(\mathbf{X}_{k,u}^{l\top} e^{-t'_u \mathbf{L}_{k,u}} \mathbf{L}_{k,u} e^{-t_u \mathbf{L}_{k,u}} \mathbf{X}_k^l \mathbf{W}_{k,u}^l)} \\ &+ 2 \underbrace{\text{tr}(\mathbf{W}_k^{l\top} \mathbf{X}_k^l e^{-t_u \mathbf{L}_{k,u}} \mathbf{L}_{k,u} e^{-t_u \mathbf{L}_{k,u}} \mathbf{X}_k^l \mathbf{W}_k^l)}_{\text{tr}(\mathbf{X}_k^{l\top} e^{-t_u \mathbf{L}_{k,u}} \mathbf{L}_{k,u} e^{-t_u \mathbf{L}_{k,u}} \mathbf{X}_k^l \mathbf{W}_k^l)} \\ &\leq e^{-2t'_d \lambda_{\min}^{(d)}} E_d(\underbrace{\mathbf{X}_{k,d}^l}_{\mathbf{B}_k^\top \mathbf{X}_{k-1}^l}) \|\mathbf{W}_{k,d}^l\|_2^2 + 2 \|\underbrace{\mathbf{X}_{k,d}^l}_{\mathbf{X}_{k,d}^l}\| \lambda_{\max}^{(d)} \|\mathbf{X}_k^l\| \|\mathbf{W}_{k,d}^l\| \|\mathbf{W}_{k,d}^{l\top}\| + e^{-2t_d \lambda_{\min}^{(d)}} E_d(\mathbf{X}_k^l) \|\mathbf{W}_{k,d}^l\|_2^2 \\ &+ e^{-2t'_u \lambda_{\min}^{(u)}} E_u(\underbrace{\mathbf{X}_{k,u}^l}_{\mathbf{B}_{k+1} \mathbf{X}_{k+1}^l}) \|\mathbf{W}_{k,u}^l\|_2^2 + 2 \|\underbrace{\mathbf{X}_{k,u}^l}_{\mathbf{X}_{k,u}^l}\| \lambda_{\max}^{(u)} \|\mathbf{X}_k^l\| \|\mathbf{W}_{k,u}^l\| \|\mathbf{W}_{k,u}^{l\top}\| + e^{-2t_u \lambda_{\min}^{(u)}} E_u(\mathbf{X}_k^l) \|\mathbf{W}_{k,u}^l\|_2^2 \\ &\leq e^{-2t'_d \lambda_{\min}(\mathbf{L}_{k,d})} E_{k-1,u}(\mathbf{X}_{k-1}^l) \lambda_{\max}(\mathbf{L}_{k-1,u}) s + 2 \|\mathbf{B}_k\| \|\mathbf{X}_k^l\| \|\mathbf{X}_{k-1}^l\| \lambda_{\max}(\mathbf{L}_{k,d}) s + e^{-2t_d \lambda_{\min}(\mathbf{L}_{k,d})} E_{k,d}(\mathbf{X}_k^l) s \\ &+ e^{-2t'_u \lambda_{\min}(\mathbf{L}_{k,u})} E_{k+1,d}(\mathbf{X}_{k+1}^l) \lambda_{\max}(\mathbf{L}_{k+1,d}) s + 2 \|\mathbf{B}_{k+1}\| \|\mathbf{X}_k^l\| \|\mathbf{X}_{k+1}^l\| \lambda_{\max}(\mathbf{L}_{k,u}) s + e^{-2t_u \lambda_{\min}(\mathbf{L}_{k,u})} E_{k,u}(\mathbf{X}_k^l) s \\ &\leq e^{-2t'_d \lambda_{\min}(\mathbf{L}_{k,d})} E_{k-1}(\mathbf{X}_{k-1}^l) \lambda_{\max}(\mathbf{L}_{k-1,u}) s + 2 \|\mathbf{X}_k^l\| \|\mathbf{X}_{k-1}^l\| \lambda_{\max}^{1.5}(\mathbf{L}_{k,d}) s \\ &+ e^{-2t'_u \lambda_{\min}(\mathbf{L}_{k,u})} E_{k+1}(\mathbf{X}_{k+1}^l) \lambda_{\max}(\mathbf{L}_{k+1,d}) s + 2 \|\mathbf{X}_k^l\| \|\mathbf{X}_{k+1}^l\| \lambda_{\max}^{1.5}(\mathbf{L}_{k,u}) s + (e^{-2t_d \lambda_{\min}(\mathbf{L}_{k,d})} + e^{-2t_u \lambda_{\min}(\mathbf{L}_{k,u})}) E_k(\mathbf{X}_k^l) s \\ &\leq e^{-2\varphi'} (E_{k-1}(\mathbf{X}_{k-1}^l) + E_{k+1}(\mathbf{X}_{k+1}^l)) \tilde{\lambda}_{\max} s + 2 \|\mathbf{X}_k^l\| (\|\mathbf{X}_{k-1}^l\| + \|\mathbf{X}_{k+1}^l\|) \tilde{\lambda}_{\max}^{1.5} s + 2e^{-2\varphi} E_k(\mathbf{X}_k^l) s, \end{aligned} \quad (39)$$

where

$$\begin{aligned} \varphi &:= \min_k \{t_d \lambda_{\min}(\mathbf{L}_{k,d}), t_u \lambda_{\min}(\mathbf{L}_{k,u})\} \\ \varphi' &:= \min_k \{t'_d \lambda_{\min}(\mathbf{L}_{k,d}), t'_u \lambda_{\min}(\mathbf{L}_{k,u})\} \\ \tilde{\lambda}_{\max} &:= \max_k \{\lambda_{\max}(\mathbf{L}_{k,d}), \lambda_{\max}(\mathbf{L}_{k,u})\} \\ s &:= \sqrt{\max_{k,l} \{\|\mathbf{W}_{k,d}^l\|, \|\mathbf{W}_{k,u}^l\|\}}. \end{aligned} \quad (40)$$

By considering $t'_d = t_d$ and $t'_u = t_u$, the proof is completed. \square

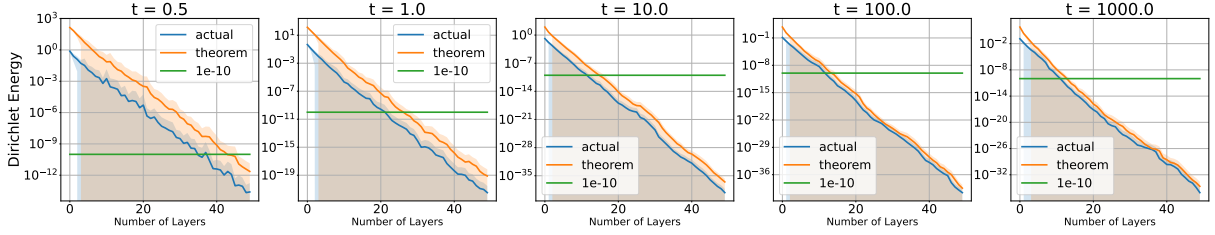


Figure 5: Over-smoothing results of COSMOS across different layer depths. Each subplot corresponds to a different parameter t in COSMOS, showing the evolution of the Dirichlet energy as a function of the number of layers.

G Proof of Corollary 5.4

Similar to the justifications mentioned in Section E for the second and third terms of the results of Theorem 5.3, the proof straightforwardly is concluded.

H Proof of Corollary 5.5

Proof. We start from $\ln s > 2\varphi$. By considering the fact that $\lambda_{\min}(\mathbf{L}_{k,d}) \leq \min(\lambda_{\min}(\mathbf{L}_{k,u}), \lambda_{\min}(\mathbf{L}_k))$, assuming $t_d = t_u = t$, replacing $\varphi = t\lambda_{\min}(\mathbf{L}_k)$, and the definition $k_f(\mathbf{L}_k) := \frac{\lambda_{\max}(\mathbf{L}_k)}{\lambda_{\min}(\mathbf{L}_k)}$ (with $\lambda_{\min}(\mathbf{L}_k) \neq 0$) [37], one can write:

$$\ln s > 2\varphi \rightarrow t < \frac{\ln s}{2\lambda_{\min}(\mathbf{L}_k)} < \frac{\ln s + 2\lambda_{\max}(\mathbf{L}_k)}{2\lambda_{\min}(\mathbf{L}_k)} < \frac{\ln s}{2\lambda_{\min}(\mathbf{L}_k)} + k_f(\mathbf{L}_k). \quad (41)$$

□

I A Deeper Look at Over-Smoothing: the Maximum Number of Layers

To study the effect of varying the Hodge receptive field t on the effective number of layers, we first generate 100 random realizations of simplices with some random (filled) holes in them using the approach introduced in [23]. Then, by fixing the number of hidden features to 4, we varied the number of layers and monitored the actual and theoretical bounds in Theorem 5.3 averaged over the random realizations. The results are shown in Figure 5. We considered a threshold of 10^{-10} as the over-smoothing occurrence threshold. As observed, increasing t reduces the effective number of layers from approximately 40 to 15. Besides, the difference between the actual and theoretical bounds gradually decreases and approaches zero, demonstrating the descriptive results of Theorem 5.3.

J Sensitivity on the Number of Branches (M) of COSMOS

Figure 6 depicts the accuracy results on the Ocean trajectory prediction task for different values of M . It is observed that increasing M up to 3 enhances the expressivity of COSMOS, as stated in Remark 4.2. However, continuing to increase beyond 3 results in performance degradation, likely due to overfitting.

K Permutation Equivariance Property of COSMOS

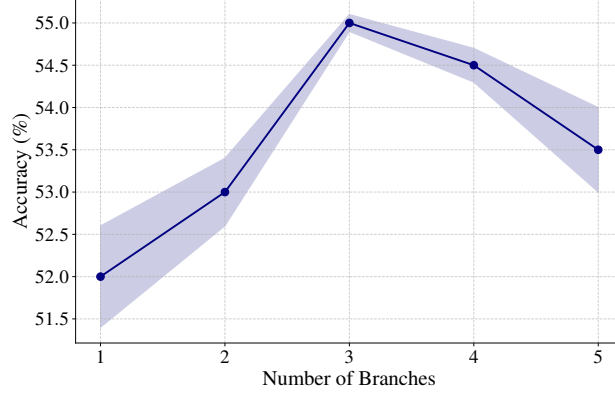
Property (Permutation equivariance [23]). Consider a simplicial complex \mathcal{X} characterized by boundary operators $\mathcal{B} = \{\mathbf{B}_k\}_{k=1}^K$. Let $\mathcal{P} = \{\mathbf{P}_k\}_{k=0}^K$ represent a sequence of permutation matrices, where each \mathbf{P}_k is of size $|\mathcal{X}_k| \times |\mathcal{X}_k|$ and corresponds to the chain complex dimensions $\{C_k\}_{k=0}^K$, ensuring $\mathbf{P}_k \in \mathbb{R}^{|\mathcal{X}_k| \times |\mathcal{X}_k|}$. We define the permuted boundary operator as

$$[PB]_k := \mathbf{P}_{k-1} \mathbf{B}_k \mathbf{P}_k^\top.$$

A simplicial convolutional network (SCN) with the learnable weight matrix \mathbf{W} is said to be permutation equivariant if, for any such transformation \mathbf{P} , the following holds:

$$\text{SCN}_{\mathbf{W}, \mathcal{B}}(\mathbf{c}_j) = \mathbf{P}_\ell \text{SCN}_{\mathbf{W}, PB}(\mathbf{P}_j \mathbf{c}_j). \quad (42)$$

Based on the above-mentioned properties, we show that COSMOS governs them in the following proposition.


 Figure 6: Sensitivity analysis on the number branches (M) of COSMOS.

Proposition K.1. *The COSMOS model stated in (11) exhibits the property of Permutation Equivariance.*

Proof. First, by considering $P\mathbf{L}_{k,d} = (\mathbf{P}_{k-1}\mathbf{B}_k\mathbf{P}_k)^\top(\mathbf{P}_{k-1}\mathbf{B}_k\mathbf{P}_k) = \mathbf{P}_k^\top\mathbf{L}_{k,d}\mathbf{P}_k$ and similarly $P\mathbf{L}_{k,u} = \mathbf{P}_k^\top\mathbf{L}_{k,u}\mathbf{P}_k$, and also $P\mathbf{X}_{k,d} = (\mathbf{P}_{k-1}\mathbf{B}_k\mathbf{P}_k^\top)^\top(\mathbf{P}_{k-1}\mathbf{X}_{k-1}) = \mathbf{P}_k\mathbf{B}_k^\top\mathbf{X}_{k-1} = \mathbf{P}_k\mathbf{X}_{k,d}$ and similarly $P\mathbf{X}_{k,u} = \mathbf{P}_k\mathbf{X}_{k,u}$, the permuted exponential expansion can be written as follows:

$$\begin{aligned}
 & \mathbf{P}_k \text{COSMOS}_{\mathbf{W},PB}(\{\mathbf{P}_{k-1}\mathbf{c}_{k-1}, \mathbf{P}_k\mathbf{c}_k, \mathbf{P}_{k+1}\mathbf{c}_{k+1}\}) \\
 &= \mathbf{P}_k \sigma \left(\mathbf{P}_k^\top e^{-t_d\mathbf{L}_{k,d}} \mathbf{X}_{k,d}^{l-1} \Theta_{k,d}^l + \mathbf{P}_k^\top e^{-t_u\mathbf{L}_{k,u}} \mathbf{X}_{k,u}^{l-1} \Theta_{k,u}^l + \mathbf{P}_k^\top e^{-t_d\mathbf{L}_{k,d}} \mathbf{X}_k^{l-1} \Psi_{k,d}^l + \mathbf{P}_k^\top e^{-t_u\mathbf{L}_{k,u}} \mathbf{X}_k^{l-1} \Psi_{k,u}^l \right) \\
 &= \sigma \left(e^{-t_d\mathbf{L}_{k,d}} \mathbf{X}_{k,d}^{l-1} \Theta_{k,d}^l + e^{-t_u\mathbf{L}_{k,u}} \mathbf{X}_{k,u}^{l-1} \Theta_{k,u}^l + e^{-t_d\mathbf{L}_{k,d}} \mathbf{X}_k^{l-1} \Psi_{k,d}^l + e^{-t_u\mathbf{L}_{k,u}} \mathbf{X}_k^{l-1} \Psi_{k,u}^l \right) \\
 &= \text{COSMOS}_{\mathbf{W},B}(\{\mathbf{c}_{k-1}, \mathbf{c}_k, \mathbf{c}_{k+1}\}),
 \end{aligned} \tag{43}$$

which completes the proof. \square